Journal of Geophysical Research

Supporting Information for

Chemical Tomography in a Fresh Wildland Fire Plume: a Large Eddy Simulation (LES) Study

Siyuan Wang,[1,2,3,*] Matthew M. Coggon,[1,2] Georgios I. Gkatzelis,[1,2,†] Carsten Warneke,[1,2] Ilann Bourgeois,[1,2] Thomas Ryerson,[2] Jeff Peischl,[1,2] Patrick R. Veres,[2] J. Andrew Neuman,[1,2] Johnathan Hair,[4] Taylor Shingler,[4] Marta Fenn,[4] Glenn Diskin,[4] L. Greg Huey,[5] Young Ro Lee,[5] Eric C. Apel,[3] Rebecca S. Hornbrook,[3] Alan J. Hills,[3] Samuel R. Hall,[3] Kirk Ullmann,[3] Megan M. Bela,[1,2] Michael K. Trainer,[1,2] Rajesh Kumar,[6] John J. Orlando,[3] Frank M. Flocke,[3] Louisa K. Emmons,[3]

[1] Cooperative Institute for Research in Environmental Sciences (CIRES), University of Colorado, Boulder, Colorado
[2] National Oceanic and Atmospheric Administration (NOAA), Chemical Sciences Laboratory (CSL), Boulder, Colorado
[3] National Center for Atmospheric Research (NCAR), Atmospheric Chemistry Observations and Modeling Laboratory (ACOM), Boulder, Colorado
[4] National Aeronautics and Space Administration, Langley Research Center, Hampton, Virginia
[5] School of Earth and Atmospheric Sciences, Georgia Institute of Technology, Atlanta, Georgia
[6] National Center for Atmospheric Research (NCAR), Research Applications Laboratory (RAL), Boulder, Colorado

* Corresponding author: Siyuan Wang (siyuan.wang@noaa.gov)
Cooperative Institute for Research in Environmental Sciences (CIRES), University of Colorado, Boulder, Boulder, Colorado
NOAA, Chemical Sciences Laboratory (CSL)
325 Broadway, Boulder, CO

† Now at: Institute of Energy and Climate Research, IEK-8: Troposphere, Forschungszentrum Jülich GmbH, Jülich, Germany

Contents of this file

- **Figures S1-S10**
- **Table S1-S3**

Section S1. WRF-LES Technical Updates.

The publicly released WRF v4.0 is used in this work. Several new updates have been released in newer versions of WRF. Two of them are relevant for this work: (1) A bug fix that improves the potential temperature tendency, which is recently implemented in WRF v4.2.2 (https://github.com/wrf-model/WRF/pull/1259/files#diff-d6fd08d956dbe380e8c1094cfc668bd4); and (2) another bug fix that improves the momentum flux and sub-grid scale stress, which is implemented in WRF v4.2.1 (https://github.com/wrf-model/WRF/pull/1214/files/323fc93b19465163ef6529e79eec5a82292e5eb1). These two new implementations are merged into the WRF model version 4.0 used in this work.

This idealized WRF-LES model is evaluated against another widely used LES model, NCAR-LES (Patton et al., 2005). In this comparision, both WRF-LES and NCAR-LES are configured in the same way (i.e., same initial conditions, driven by the same surface heat and moisture fluxes). It drew our attention that the friction velocity (U_*) calculated using this WRF-LES (with the aforementioned bug fixes) is roughly a factor of two lower than that calculated using NCAR-LES. The reason may be that, in the default WRF, the friction velocity is calculated using the bulk Richardson number, which may not be properly updated in idealized WRF-LES when the surface heat flux is prescribed (personal communication: Jimy Dudhia, National Center for Atmospheric Research). Therefore, a new friction velocity scheme is developed in this work for the idealized WRF-LES to solve U_* directly:

$$U_* = \frac{\kappa U}{\ln(\frac{z}{z_0}) - \Psi_m(\frac{z}{L})} \qquad \text{Equation S1}$$

$$L = -\frac{\rho C_p \theta U_*^3}{kgH} \qquad \text{Equation S2}$$

Where κ is the von Kármán constant, U is the surface horizontal wind speed (m s^{-1}), z_0 is the roughness length scale (m), Ψ_m is the stability correction function for momentum (in the WRF surface layer scheme), L is the Obukhov length (m), ρ is the air density (kg m^{-3}), C_p is the heat capacity (1005 J kg^{-1} K^{-1}), ϑ is the potential temperature (K), H is the surface heat flux (W m^{-2}), and g is the acceleration due to gravity (9.8 m s^{-2}),. Equations S1 and S2 are solved implicitly using the Newton iteration method. Using this new scheme, the friction velocity calculated in this idealized WRF-LES driven by surface heat fluxes is greatly improved and in very good agreement with the NCAR-LES.

Other major physical and dynamical settings of the WRF-LES model are summarized as follows: microphysics option: Morrison 2-moment scheme (mp_physics = 10);

longwave/shortwave radiation option: Rapid Radiative Transfer Model for GCMs (RRTMG; ra_lw_physics/ra_sw_physics = 4); turbulence and mixing option: evaluates mixing terms in physical space (stress form; diff_opt = 2); eddy coefficient option: 1.5 order TKE closure (km_opt = 2).

Section S2. Mesoscale WRF-Chem

A mesoscale WRF-Chem simulation (12 km horizontal resolution) was used to generate the initial conditions for the WRF-LES model (Figures S1 and S2). Some of the major settings of this 12 km WRF-Chem simulation are summarized as follows: microphysics option: Morrison 2-moment scheme (mp_physics = 10); longwave/shortwave radiation option: Rapid Radiative Transfer Model for GCMs (RRTMG; ra_lw_physics/ra_sw_physics = 4); turbulence and mixing option: evaluates mixing terms in physical space (stress form; diff_opt = 2); eddy coefficient option: horizontal Smagorinsky first order closure (km_opt = 4); surface-layer option: MYNN surface layer (sf_sfclay_physics = 5); land-surface option: Noah Land-Surface Model (sf_surface_physics = 2); boundary-layer option: MYNN 2.5 level TKE scheme (bl_pbl_physics = 5); cumulus option: Grell-Devenyi ensemble scheme (cu_physics = 3); chemistry option: NOAA/ESRL RACM chemical mechanism (chem_opt = 108); photolysis option: Madronich photolysis (TUV; phot_opt = 1).

Table S1. The highly simplified chemical mechanism used in the WRF-LES model. This mechanism is condensed based on T1 MOZART in the WRF package (Knote et al., 2014).

Reactions	Rate coefficients
O3 = 2 OH	O3_hv_H2O(T, [M], [H2O], j_O1D), note 1
NO2 + hv = NO + O3	FTUV
NO2 + aerosols = 0.5 HNO2	$\gamma = 5\times10^{-4}$, note 2
HNO2 + hv = OH + NO	FTUV
H2O2 + hv = 2 OH	FTUV
HCHO + hv = 2 HO2 + CO	FTUV
HCHO + hv = CO	FTUV
OH + HO2 = H2O	T1 MOZART
OH + O3 = HO2	T1 MOZART
HO2 + HO2 = H2O2	T1 MOZART
HO2 + O3 = OH	T1 MOZART
NO + O3 = NO2	T1 MOZART
NO2 + OH =	T1 MOZART
NO2 + O3 = NO3	T1 MOZART
NO + HO2 = NO2 + OH	T1 MOZART
NO2 + NO3 = N2O5	T1 MOZART
NO + NO3 = NO2 + NO2	T1 MOZART
HO2 + NO3 = OH + NO2	T1 MOZART
N2O5 = NO2 + NO3	T1 MOZART
N2O5 =	T1 MOZART
NO3 + hv = 0.11 NO + 0.89 NO2 + 0.89 O3	FTUV
CH3O2 + NO = HCHO + 0.99 NO2 + HO2	T1 MOZART
CH3O2 + HO2 =	T1 MOZART
CO + OH = HO2	T1 MOZART
CH4 + OH = CH3O2	T1 MOZART
HCHO + OH = HO2 + CO	T1 MOZART
C3H6 + OH = PO2	T1 MOZART
PO2 + NO = HO2 + HCHO + ALDS + NO2	T1 MOZART
PO2 + HO2 = POOH	T1 MOZART
POOH + OH = 0.5 PO2 + 0.5 OH + 0.5 ALDS	T1 MOZART
C3H6 + O3 = 0.5 HCHO + 0.5 ALDS + 0.28 CH3O2 + 0.28 HO2 + 0.36 OH	T1 MOZART
C3H6 + NO3 = NO2 + ALDS	T1 MOZART
ISOP + OH = ISOPO2	T1 MOZART
ISOP + O3 = 0.6 MVKMACR + 0.27 OH + 0.06 HO2 + 0.6 HCHO + 0.3 CO + 0.1 O3 + 0.2 RCO3	T1 MOZART, note 3
ISOP + NO3 = ISOPNO3	T1 MOZART
ISOPO2 + NO = 0.08 ONITR + 0.92 NO2 + 0.55 MVKMACR + 0.37 ALDS + 0.55 HCHO + HO2	T1 MOZART
ISOPO2 + HO2 = ISOPOOH	T1 MOZART

ISOPO2 + CH3O2 = HO2 + 1.2 HCHO + 0.45 MVKMACR + 0.3 ALDS	T1 MOZART
ISOPOOH + OH = 0.5 XO2 + 0.5 ISOPO2	T1 MOZART
ISOPOOH + hv = 0.69 MVKMACR + 0.69 HCHO + HO2	FTUV
MACRO2 + NO = NO2 + 0.47 HO2 + 0.25 HCHO + ALDS + 0.53 RCO3 + 0.22 CO	T1 MOZART
MACRO2 + HO2 =	T1 MOZART
MACRO2 + CH3O2 = 0.73 HO2 + 0.88 HCHO + 0.11 CO + 0.73 ALDS + 0.26 RCO3	T1 MOZART
MVKMACR + hv = 0.165 OH + 0.335 HO2 + 0.65 RCO3 + 0.335 HCHO + 0.685 CO + 0.15 CH3O2	T1 MOZART
MVKMACR + OH = 0.75 MACRO2 + 0.25 RCO3	T1 MOZART
MVKMACR + O3 = 0.75 HCHO + 0.895 ALDS + 0.148 OH + 0.2 O3 + 0.168 HO2 + 0.125 CO	T1 MOZART
ONITR + hv = HO2 + CO + NO2 + HCHO	T1 MOZART
ONITR + OH = ALDS + HO2 + 0.4 NO2	T1 MOZART
ALDS + OH = RCO3	T1 MOZART, note 4
ALDS + hv = CH3O2 + CO + HO2	j-CH3CHO in FTUV
XO2 + NO = NO2 + 1.5 HO2 + CO + 0.75 ALDS	T1 MOZART
XO2 + HO2 =	T1 MOZART
XO2 + CH3O2 = HO2 + 0.7 HCHO + 0.4 CO + 0.3 ALDS	T1 MOZART
RCO3 + NO = NO2 + HCHO	T1 MOZART
RCO3 + HO2 = 0.25 O3	T1 MOZART
RCO3 + CH3O2 = 2 HCHO + HO2	T1 MOZART
RCO3 + NO2 = PAN	T1 MOZART
PAN = RCO3 + NO2	T1 MOZART
PAN + hv = 0.8 RCO3 + 0.8 NO2 + 0.2 CH3O2 + 0.2 NO3	j-PAN in FTUV
ISOPNO3 + NO = 1.206 NO2 + 0.794 HO2 + 0.072 HCHO + 0.206 MVKMACR + 0.794 ONITR	T1 MOZART
ISOPNO3 + HO2 = 0.206 NO2 + 0.206 OH + 0.206 HCHO + 0.206 MVKMACR + 0.794 ONITR	T1 MOZART
BENZENE + OH = 0.83 HO2 + 0.18 CO + 0.35 BENZO2	T1 MOZART
BENZO2 + HO2 = BENZOOH	T1 MOZART
BENZO2 + NO = NO2 + 0.5 ALDS + HO2	T1 MOZART
BENZOOH + OH = BENZO2	T1 MOZART
TOLUENE + OH = 0.65 TOLO2 + 0.05 RCO3 + 0.38 HO2 + 0.15 CO	T1 MOZART
TOLO2 + HO2 = TOLOOH	T1 MOZART
TOLO2 + NO = NO2 + 0.6 ALDS + HO2	T1 MOZART
TOLOOH + OH = TOLO2	T1 MOZART
FURAN + OH = 0.39 DIAL + 0.49 HO2 + 0.51 FURANO2	Coggon et al., 2019
DIAL + OH = DIALO2	Coggon et al., 2019
DIALO2 + NO = NO2 + 0.49 MALANHY + 0.96 HO2 + 0.04 CH3O2	Coggon et al., 2019
DIALO2 + NO2 =	Coggon et al., 2019
DIAL + hv = 0.74 DIALO2 + 0.74 HO2 + 0.34 CO	0.098*j_{NO2}, Coggon et al., 2019

FURANO2 + NO = NO2 + FURANONE + 0.81 HO2 + 0.19 CH3O2	Coggon et al., 2019
FURANONE + OH = 0.69 MALANHY + 0.66 HO2 + 0.34 CH3O2 + 0.43 CO	Coggon et al., 2019
FURAN + O3 =	Coggon et al., 2019
FURAN + NO3 =	Coggon et al., 2019

Note 1: O3_hv_H2O(T, [M], [H2O], j_O1D) = 1.63E-10*EXP(60/T)*[H2O]* j_O1D / (1.63E-10*EXP(60/T)* [H2O] + 2.15E-11*EXP(110/T)*0.79*[M] + 3.30E-11*EXP(55/T)*0.21*[M]), where T is temperature (K), and [M] and [H2O] are air and water vapor concentrations (molecules cm^{-3}), respectively. This approach assumes steady-state for O^1D.

Note 2: the reactive uptake coefficient of NO2 is estimated from based on the literature values (Ammann et al., 2013). Aerosol surface area in this work considers only BC and OC.

Note 3: MVKMACR is the sum of MVK and MACR.

Note 4: ALDS is a lumped species for aldehydes including acetaldehyde, glycolaldehyde, hydroxyacetone, as well as lumped unsaturated hydroxycarbonyl from T1 MOZART. Of all these lumped species, acetaldehyde is the most dominant one in fire plumes, therefore the kinetics of acetaldehyde (e.g., photolysis frequency, OH rate coeffcieint) are used for the removal of ALDS.

Table S2. Fire emissions used in the WRF-LES model. These emissions are adjusted until reasonable agreements are achieved when compared to airborne measurements (Figure 3).

Species	Fire emission	Unit
NO	1097	ppb m s^{-1}
CO	77780	ppb m s^{-1}
ISOP	238	ppb m s^{-1}
MVKMACR	153	ppb m s^{-1}
EC	297	µg m^{-2} s^{-1}
OC	19649	µg m^{-2} s^{-1}
C3H6	802	ppb m s^{-1}
ALDS	560	ppb m s^{-1}
HNO2	123	ppb m s^{-1}
HCHO	930	ppb m s^{-1}
TOLUENE	129	ppb m s^{-1}
BENZENE	259	ppb m s^{-1}
FURAN	387	ppb m s^{-1}

Table S3. NASA DC-8 airborne measurements used in this work. The NASA Langley Research Center Online Custom Data Merging Tool (beta 1.4, https://www-air.larc.nasa.gov/cgi-bin/Driver.cgi?operation=doMerge) is used to generate the 1-Hz merge dataset, except for the DIAL data.

Measurements	Instrument	Reference
532 nm backscatter ratio	NASA Differential Absorption LIDAR (DIAL)	(Hair et al., 2008)
Ozone (O_3), nitrogen oxides (NO_x)	NOAA NOyO3 4-channel chemiluminescence	(Ryerson et al., 2000)
Photolysis frequencies (j-values)	NCAR CCD Actinix Flux Spectroradiometers (CAFS)	(Shetter & Müller, 1999)
Carbon monoxide (CO)	NASA Differential Absorption Carbon monOxide Measurement (DACOM)	(Warner et al., 2010)
Nitrous acid (HONO)	NOAA Iodide Time-of-Flight Chemical Ionization Mass Spectrometer (ToF CIMS)	(Neuman et al., 2016; Veres et al., 2020)
Peroxyacetyl nitrate (PAN)	GeorgiaTech chemical ionization mass spectrometer (CIMS)	(Huey, 2007)
Formaldehyde (HCHO)	NASA In Situ Airborne Formaldehyde (ISAF)	(Cazorla et al., 2015)
Black carbon (BC)	NOAA Single-Particle Soot Photometer (SP2)	(Schwarz et al., 2006)
Organic aerosol (OA), Organic Aerosol-to-organic carbon ratio (OA/OC Ratio)	CU High Resolution Time-of-Flight Aerosol Mass Spectrometer (HR-AMS)	(DeCarlo et al., 2006)
Ethane	CU Compact Atmospheric Multispecies Spectrometer (CAMS)	(P. Weibring et al., 2006; Petter Weibring et al., 2007)
Propane, i-butane, n-butane, i-pentane, n-pentane, i-butene/1-butene, isoprene, MVK, MACR, MEK, furan, 2-methylfuran,3-methylfuran, furfural	NCAR Trace Organic Gas Analyzer (TOGA)	(Apel et al., 2015; Wang et al., 2019)
Benzene, toluene, acetaldehyde, methanol, ethanol, acrolein, acetone/propanal, maleic anhydride, phenol, styrene	NOAA Proton-Transfer Reaction Time-of-Flight Mass Spectrometry (PTR-ToF-MS)	(Yuan et al., 2016)

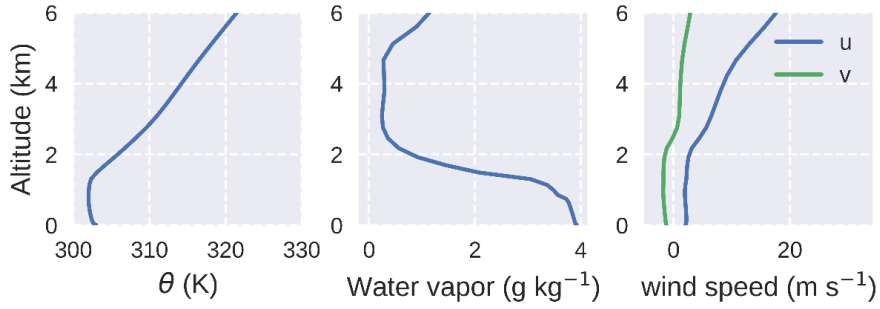

Figure S1. The vertical profiles of potential temperature (θ), water vapor, and wind used to initialize the LES model. These profiles are derived from the 12-km mesoscale WRF-Chem simulation (Section S2).

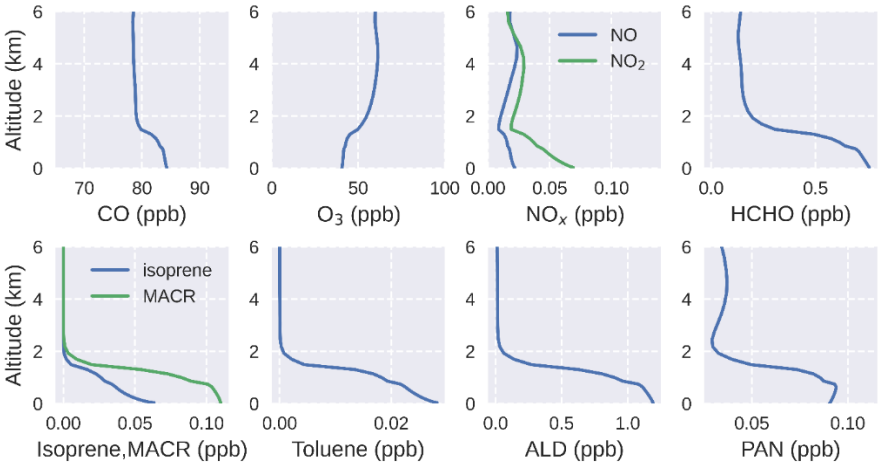

Figure S2. The vertical profiles of chemicals used to initialize the LES model. These profiles are derived from the 12-km mesoscale WRF-Chem simulation (Section S2).

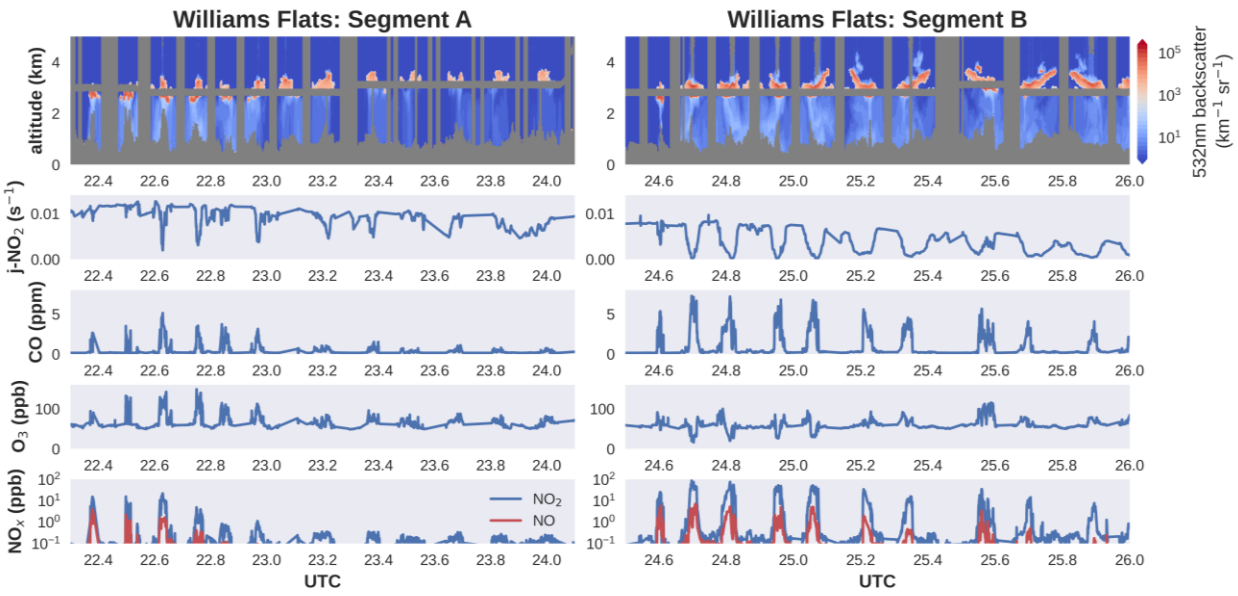

Figure S3. Selected airborne measurements collected during the "in-plume" Segments A and B.

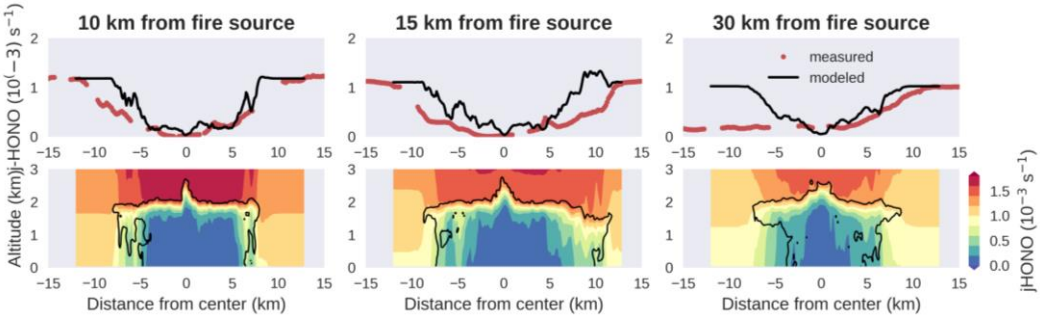

Figure S4. Measured j-HONO (top) during Segment B and modeled j-HONO across sections (bottom) at 10 km, 15 km, and 30 km downwind of the fire source. Also shown in the top panel are the modeled j-HONO sampled at the same distance from the fire, at 2 km above the model surface.

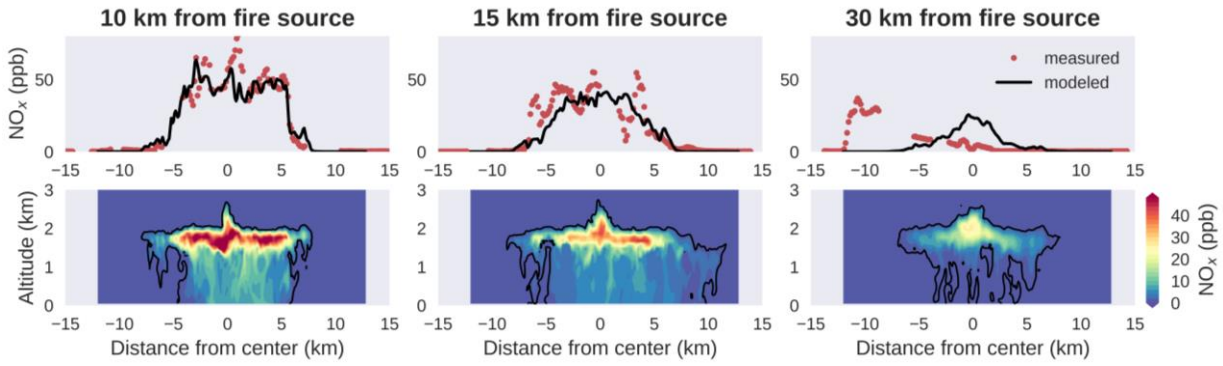

Figure S5. Same as Figure S4 but for NO_x.

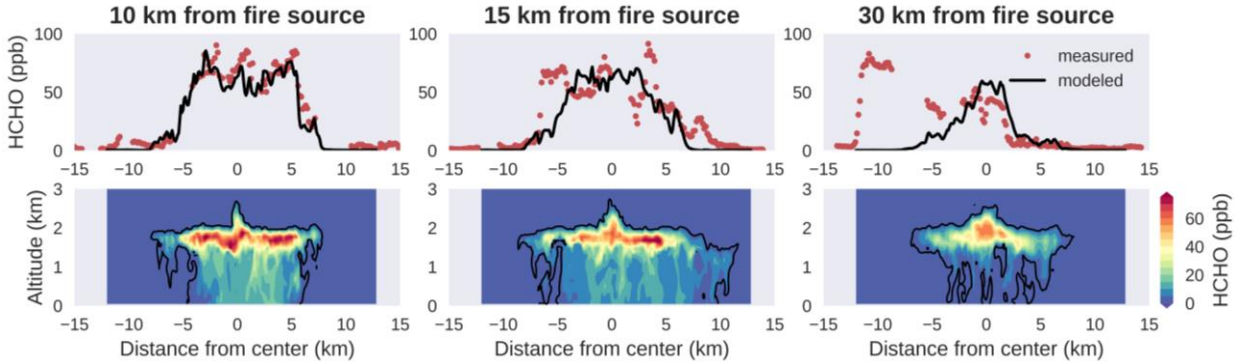

Figure S6. Same as Figure S4 but for HCHO.

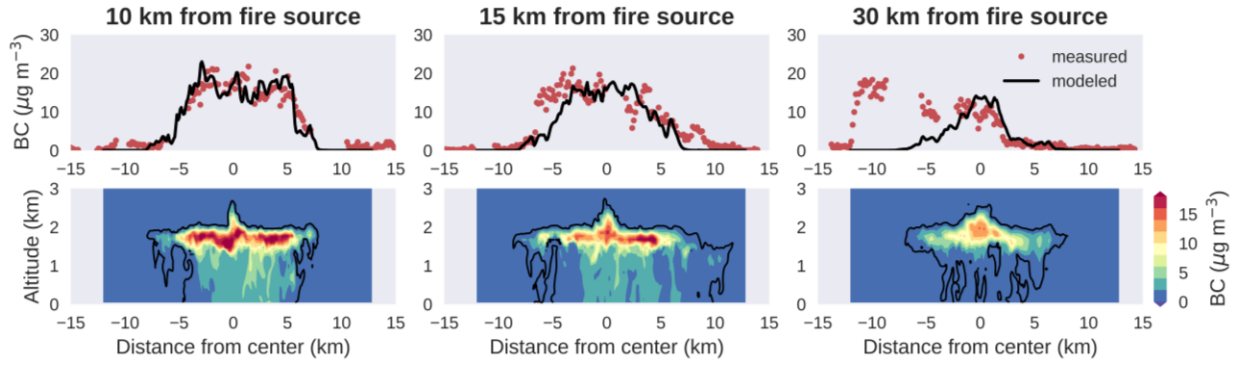

Figure S7. Same as Figure S4 but for BC.

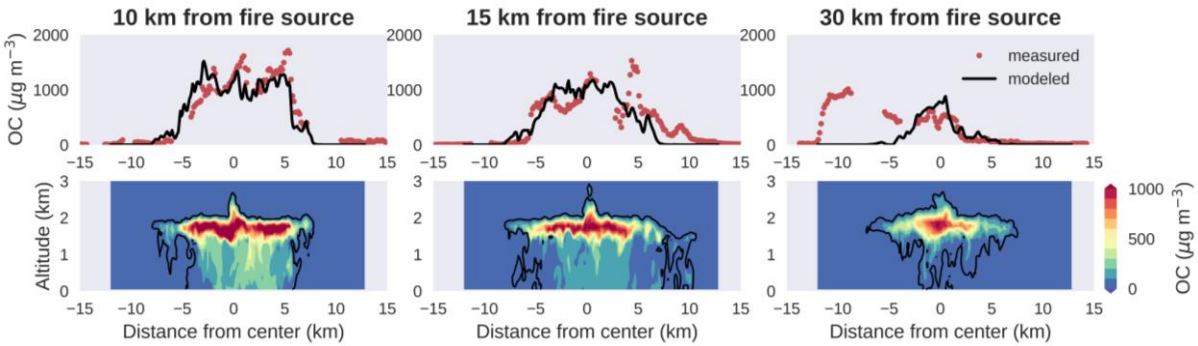

141

142 Figure S8. Same as Figure S4 but for OC. OC is calculated from CU HR-AMS measured OA and
143 OA/OC Ratio.

144

145

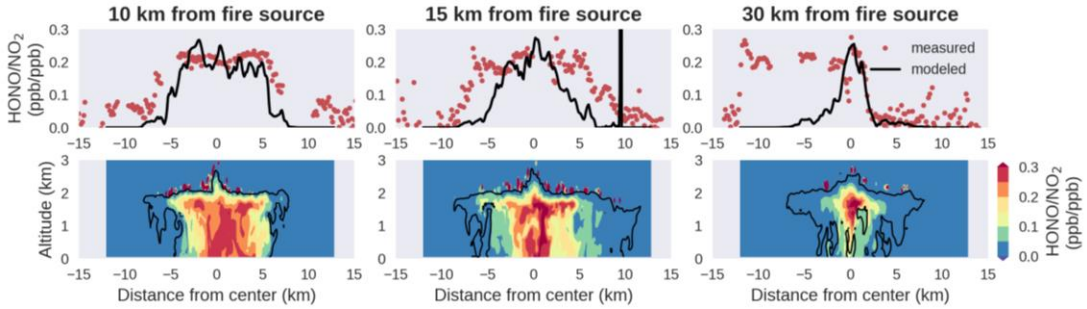

146

147 Figure S9. Same as Figure S4 but for the ratio between HONO and NO_2 (ppb ppb^{-1}).

148

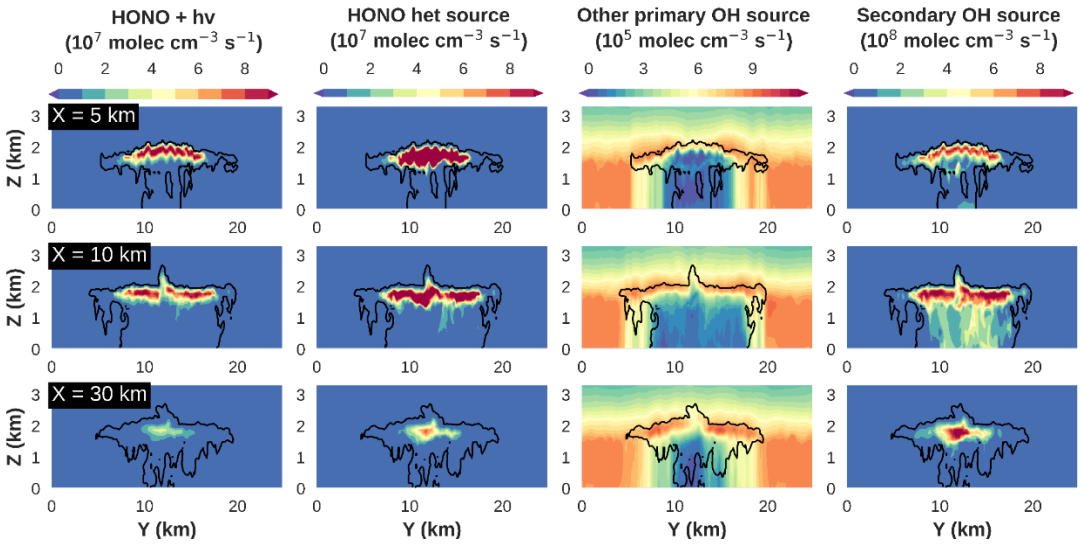

Figure S10. Modeled plume cross sections of HONO photolysis, heterogeneous HONO production, other primary OH source (mostly photolysis of O_3 and aldehydes), and secondary OH source, at X = 5, 10, and 30 km.

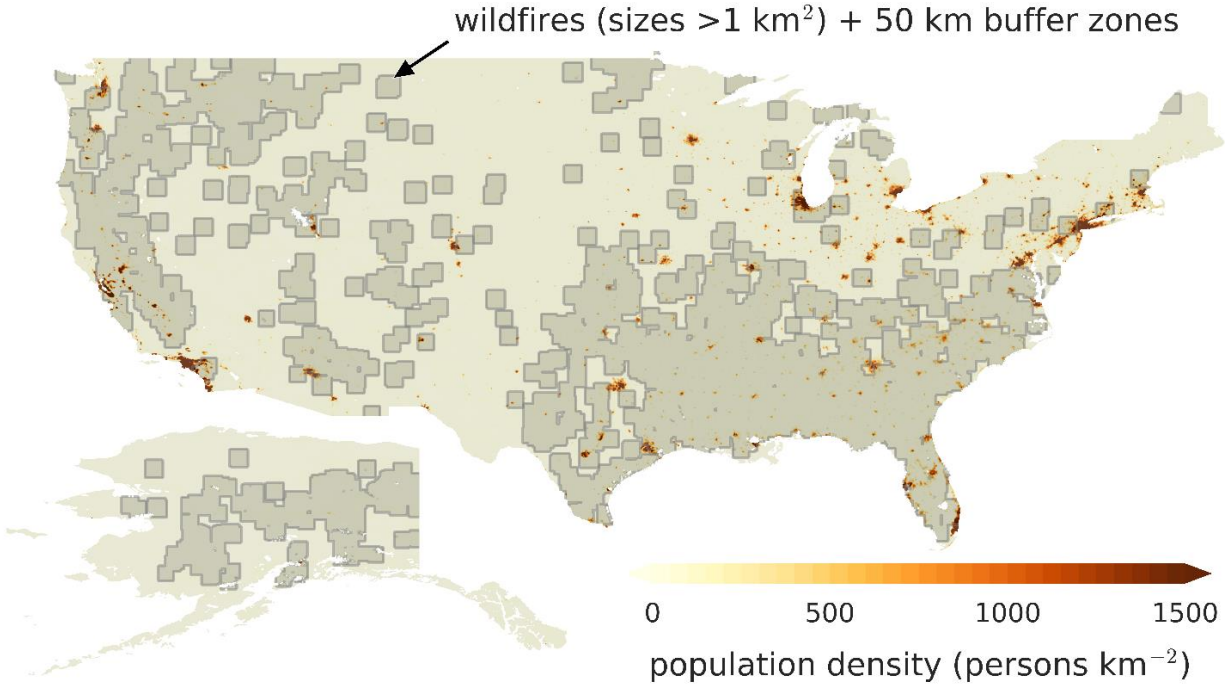

Figure S11. U.S. wildfires in 2019 larger than 1 km^2 (fire size) with 50 km buffer zones (grey patches) overlaid on the U.S. population density map. The wildfire sizes are reported in FINN version 2. The gridded U.S. population density map is from (Center for International Earth Science Information Network, Columbia University, 2020).

References

Ammann, M., Cox, R. A., Crowley, J. N., Jenkin, M. E., Mellouki, A., Rossi, M. J., et al. (2013). Evaluated kinetic and photochemical data for atmospheric chemistry: Volume VI – heterogeneous reactions with liquid substrates. *Atmospheric Chemistry and Physics*, *13*(16), 8045–8228. https://doi.org/10.5194/acp-13-8045-2013

Apel, E., Hornbrook, R., Hills, A., Blake, N., Barth, M., Weinheimer, A., et al. (2015). Upper tropospheric ozone production from lightning NOx-impacted convection: Smoke ingestion case study from the DC3 campaign. *Journal of Geophysical Research: Atmospheres*, *120*(6), 2505–2523. https://doi.org/10.1002/2014JD022121

Cazorla, M., Wolfe, G. M., Bailey, S. A., Swanson, A. K., Arkinson, H. L., & Hanisco, T. F. (2015). A new airborne laser-induced fluorescence instrument for in situ detection of formaldehyde throughout the troposphere and lower stratosphere. *Atmos. Meas. Tech.*, *8*(2), 541–552. https://doi.org/10.5194/amt-8-541-2015

Center for International Earth Science Information Network, Columbia University. (2020). *Gridded Population of the World, Version 4 (GPWv4): Population Density Revision UN WPP Country Totals, Revision 11*. Palisades, NY: NASA Socioeconomic Data and Applications Center (SEDAC). Retrieved from https://doi.org/10.7927/H4F47M65

Coggon, M. M., Lim, C. Y., Koss, A. R., Sekimoto, K., Yuan, B., Gilman, J. B., et al. (2019). OH chemistry of non-methane organic gases (NMOGs) emitted from laboratory and ambient biomass burning smoke: evaluating the influence of furans and oxygenated aromatics on ozone and secondary NMOG formation. *Atmospheric Chemistry and Physics*, *19*(23), 14875–14899. https://doi.org/10.5194/acp-19-14875-2019

DeCarlo, P. F., Kimmel, J. R., Trimborn, A., Northway, M. J., Jayne, J. T., Aiken, A. C., et al. (2006). Field-deployable, high-resolution, time-of-flight aerosol mass spectrometer. *Analytical Chemistry*, *78*(24), 8281–8289.

Hair, J. W., Hostetler, C. A., Cook, A. L., Harper, D. B., Ferrare, R. A., Mack, T. L., et al. (2008). Airborne High Spectral Resolution Lidar for profiling aerosol optical properties. *Applied Optics*, *47*(36), 6734–6752. https://doi.org/10.1364/AO.47.006734

Huey, L. G. (2007). Measurement of trace atmospheric species by chemical ionization mass spectrometry: Speciation of reactive nitrogen and future directions. *Mass Spectrometry Reviews*, *26*(2), 166–184. https://doi.org/10.1002/mas.20118

Knote, C., Hodzic, A., Jimenez, J. L., Volkamer, R., Orlando, J. J., Baidar, S., et al. (2014). Simulation of semi-explicit mechanisms of SOA formation from glyoxal in aerosol in a 3-D model. *Atmospheric Chemistry and Physics*, *14*(12), 6213–6239.

Neuman, J. A., Trainer, M., Brown, S. S., Min, K.-E., Nowak, J. B., Parrish, D. D., et al. (2016). HONO emission and production determined from airborne measurements over the Southeast U.S. *Journal of Geophysical Research: Atmospheres*, *121*(15), 9237–9250. https://doi.org/10.1002/2016JD025197

Patton, E. G., Sullivan, P. P., & Moeng, C.-H. (2005). The Influence of Idealized Heterogeneity on Wet and Dry Planetary Boundary Layers Coupled to the Land Surface. *Journal of Atmospheric Sciences*, *62*(7), 2078–2097. https://doi.org/10.1175/JAS3465.1

Ryerson, T., Williams, E., & Fehsenfeld, F. (2000). An efficient photolysis system for fast-response NO2 measurements. *Journal of Geophysical Research: Atmospheres*, *105*(D21), 26447–26461. https://doi.org/10.1029/2000JD900389

205 Schwarz, J. P., Gao, R. S., Fahey, D. W., Thomson, D. S., Watts, L. A., Wilson, J. C., et al. (2006). Single-
206 particle measurements of midlatitude black carbon and light-scattering aerosols from the
207 boundary layer to the lower stratosphere. *Journal of Geophysical Research: Atmospheres*,
208 *111*(D16). https://doi.org/10.1029/2006JD007076
209 Shetter, R. E., & Müller, M. (1999). Photolysis frequency measurements using actinic flux
210 spectroradiometry during the PEM-Tropics mission: Instrumentation description and some
211 results. *Journal of Geophysical Research: Atmospheres*, *104*(D5), 5647–5661.
212 https://doi.org/10.1029/98JD01381
213 Veres, P. R., Neuman, J. A., Bertram, T. H., Assaf, E., Wolfe, G. M., Williamson, C. J., et al. (2020). Global
214 airborne sampling reveals a previously unobserved dimethyl sulfide oxidation mechanism in the
215 marine atmosphere. *Proceedings of the National Academy of Sciences*, *117*(9), 4505–4510.
216 https://doi.org/10.1073/pnas.1919344117
217 Wang, S., Hornbrook, R. S., Hills, A., Emmons, L. K., Tilmes, S., Lamarque, J.-F., et al. (2019). Atmospheric
218 Acetaldehyde: Importance of Air-Sea Exchange and a Missing Source in the Remote
219 Troposphere. *Geophysical Research Letters*. https://doi.org/10.1029/2019GL082034
220 Warner, J. X., Wei, Z., Strow, L. L., Barnet, C. D., Sparling, L. C., Diskin, G., & Sachse, G. (2010). Improved
221 agreement of AIRS tropospheric carbon monoxide products with other EOS sensors using
222 optimal estimation retrievals. *Atmospheric Chemistry and Physics*, *10*(19), 9521–9533.
223 https://doi.org/10.5194/acp-10-9521-2010
224 Weibring, P., Richter, D., Fried, A., Walega, J. G., & Dyroff, C. (2006). Ultra-high-precision mid-IR
225 spectrometer II: system description and spectroscopic performance. *Applied Physics B*, *85*(2),
226 207–218. https://doi.org/10.1007/s00340-006-2300-4
227 Weibring, Petter, Richter, D., Walega, J. G., & Fried, A. (2007). First demonstration of a high performance
228 difference frequency spectrometer on airborne platforms. *Optics Express*, *15*(21), 13476–13495.
229 https://doi.org/10.1364/OE.15.013476
230 Yuan, B., Koss, A., Warneke, C., Gilman, J. B., Lerner, B. M., Stark, H., & de Gouw, J. A. (2016). A high-
231 resolution time-of-flight chemical ionization mass spectrometer utilizing hydronium ions (H_3O^+
232 ToF-CIMS) for measurements of volatile organic compounds in the atmosphere. *Atmospheric*
233 *Measurement Techniques*, *9*(6), 2735–2752. https://doi.org/10.5194/amt-9-2735-2016
234